

We are IntechOpen, the world's leading publisher of Open Access books Built by scientists, for scientists

6,900

Open access books available

186,000

International authors and editors

200M

Downloads

Our authors are among the

154

Countries delivered to

TOP 1%

most cited scientists

12.2%

Contributors from top 500 universities



WEB OF SCIENCE™

Selection of our books indexed in the Book Citation Index
in Web of Science™ Core Collection (BKCI)

Interested in publishing with us?
Contact book.department@intechopen.com

Numbers displayed above are based on latest data collected.
For more information visit www.intechopen.com



Small-Angle Scattering from Mass and Surface Fractals

Eugen Mircea Anitas

Additional information is available at the end of the chapter

<http://dx.doi.org/10.5772/intechopen.70870>

Abstract

The concepts of mass and surface fractals are introduced, and the corresponding small-angle scattering (SAS; X-rays, neutrons) intensities are computed. It is shown how to resolve the fractal structure of various complex systems from experimental scattering measurements, and how obtained data are related to specific features of the fractal models. We present and discuss various mass and surface fractal structures, including fractals generated from iterated function systems and cellular automata. In addition to the fractal dimension and the overall fractal size, the suggested analysis allows us to obtain the iteration number, the number of basic units which form the fractal and the scaling factor.

Keywords: small-angle scattering, form factor, structure factor, fractals, iterated function system, cellular automata

1. Introduction

A great number of natural systems provide us with examples of nano- and micro- structures, which appear similar under a change of scale. These structures are called fractals [1], and can be observed in various disordered materials, rough surfaces, aggregates, metals, polymers, gels, colloids, thin films, etc. Quite often, the physical properties (mechanical, optical, statistical, thermodynamical, etc.) depend on their spatial configurations, and a great deal of activity has been performed in elucidating such correlations [2–4]. To this aim, in the last decade, important steps have been performed in three directions: instrumentation [5–7], computer programs [8, 9], and the development of new methods for sample preparation [10–14]. The first two have been proved to be very useful for the physical execution and data analysis, and the third one for preparation of nano- and micro-materials with the pre-defined structure and functions.

These achievements have stimulated a great interest in the development of theoretical investigations for structural modeling of self-similar objects at nano- and micro-scale. In particular, models based on deterministic or exact self-similar fractals (i.e., fractals that are self-similar at every point, such as the Koch snowflake, Cantor set, or Mandelbrot cube) have been frequently

used, since this type of fractals allows an analytical representation of various geometrical parameters (radius of gyration) or of the scattering intensity spectrum. Although for most fractals generated by natural processes, this is only an approximation, in the case of deterministic nano- and micro-materials obtained recently such as 2D Sierpinski gaskets [15] and Cantor sets [16], or 3D Menger sponge [17] and octahedral structures [18], this approximation becomes exact.

Small-angle scattering of X-rays (SAXS) and/or neutrons (SANS) are well established techniques for probing the nano/micro scale structure in disordered materials [19–21]. While in the case of X-rays, the scattering is mostly determined by the interaction of the incident radiation with electrons, in the case of neutrons, the scattering is determined by their interaction with the atomic nuclei and with the magnetic moments in magnetic materials. Since the wavelengths of X-rays (0.5–2 Å) are of the same order of magnitude as those of thermal neutrons (1–10 Å), often, the data analysis and interpretation procedures for SANS can be interchanged with SAXS, and the developed theoretical models can be applied, generally, to both techniques [22]. However, using neutrons is very important in studying magnetic properties of materials as well as in emphasizing or concealing certain features of the investigated sample [23]. In the later case, the possibility of wide variations in the neutron scattering lengths (which can be negative sometimes) is exploited, and this is a unique feature of SANS, which makes it a preferred method over SAXS in structural analysis of biological materials [24, 25].

As compared with other methods of structural investigations, SAXS/SANS have the advantage that they are noninvasive, the physical quantities of interest (specific surface, radius of gyration, volume, or the fractal dimension) are averaged over a macroscopic volume and they can be extracted with almost no approximation [26]. In particular, for self-similar objects (either exact or statistical), the most important advantage is that SAXS/SANS can distinguish between mass [27] and surface fractals [28]. Experimentally, the difference is revealed through the value of the scattering exponent τ in the region where the scattering intensity $I(q)$ decays as a power-law, i.e., $I(q) \propto q^{-\tau}$, where $q = (4\pi/\lambda) \sin \theta$ is the scattering vector, λ is the wavelength of the incident radiation, and 2θ is the scattering angle. For mass fractals $\tau = D_m$, where D_m is the mass fractal dimension with $0 < D_m < 3$. For surface fractals $\tau = 6 - D_s$, where D_s is the surface fractal dimension with $2 < D_s < 3$. Thus, in practice if the absolute value of the measured scattering exponent is smaller than 3, the sample is a mass fractal with fractal dimension τ (in the measured q -range), and if the exponent is between 3 and 4, the sample is a surface fractal with fractal dimension $6 - \tau$.

Besides the fractal dimension (either mass or surface one), traditionally from SAXS/SANS patterns, we can also obtain the overall size of the fractal, as well as the size of the basic structural units composing the fractal. The last years have brought a breakthrough in the theoretical analysis of SAXS/SANS experimental data, allowing for the extraction of additional structural information and detailed modeling of fractals using a deterministic approach [29–40]. This progress was stimulated by recent advances in nanotechnology, which allows preparation of both mass and surface deterministic fractals at sub-micrometer scale [15–18, 41, 42], as well as by instrumentation which allows novel structural features to be recorded in experimental data [43].

This chapter focuses on the interpretation of SAXS/SANS data from deterministic mass and surface fractals. First, a brief theoretical background on the basics of SAS theory, and on description of mass and surface fractals, is presented. Here, we also include the theory of some well-known methods of generating fractals, such as iterated function system of cellular automata. Novel data analysis methods for extracting additional structural information are presented and illustrated by applications to various models of mass and surface fractals.

2. Theoretical background

In this section, some important concepts for the analysis of SAXS/SANS are reviewed, and analytical and numerical procedures for calculating the scattering intensity from some basic geometrical shapes are described. As we will see in the next section, these geometrical shapes will form the “scattering units” of the fractals. Then, the basic notions of fractal theory including fractal dimension, mass, and surface fractals are presented and defined in a rigorous manner, and two general methods for generating fractal structures are presented. These concepts are then applied in calculating the SAXS/SANS patterns from several theoretical models of mass and surface fractals.

2.1. Small-angle scattering

2.1.1. General remarks

In a SAS experiment, a beam of X-rays or neutrons is emitted from a source and strikes the sample. A small fraction is scattered by the sample and is recorded by the detector. In **Figure 1**, the incident beam has a wave vector k_i , and the scattered beam with the wave vector k_s makes the angle 2θ with the direction of the incoming or transmitted beam.

To describe the scattering from assemblies of objects with scattering length b_j , we write the scattering length density *SLD* as $\rho(\mathbf{r}) = \sum_j b_j \delta(\mathbf{r} - \mathbf{r}_j)$ [21], where \mathbf{r}_j is the object positions. Then, the total scattering amplitude is defined by the Fourier transform of $\rho(\vec{r})$:

$$A(\mathbf{q}) \equiv \int_v \rho(\mathbf{r}) e^{-i\mathbf{q}\cdot\mathbf{r}} d^3r, \quad (1)$$

where v is the total volume irradiated by the beam. In the following, we consider scattering occurring in a particulate system where particles of density ρ_m are dispersed in a uniform solid matrix of density ρ_p . Then, the excess scattering *SLD* is defined by $\Delta\rho = \rho_m - \rho_p$. We also consider that the objects are fractals that are randomly distributed and with uncorrelated positions and orientations. Thus, the scattering intensities of each object are added, and the intensity from the entire sample can be obtained from a single object averaged over all orientations, according to [29]:

$$I(q) = n|\Delta\rho|^2V^2\langle|F(\mathbf{q})|^2\rangle, \quad (2)$$

where n is the concentration of objects, V is the volume of each object, and $F(\vec{q})$ is the normalized scattering amplitude given by:

$$F(\mathbf{q}) = \frac{1}{V} \int_V e^{-i\mathbf{q}\cdot\mathbf{r}} d^3r. \quad (3)$$

The symbol $\langle \dots \rangle$ stands for ensemble averaging over all orientations, and for an arbitrary function f , it is calculated according to:

$$\langle f(q_x, q_y, q_z) \rangle = \frac{1}{4\pi} \int_0^\pi d\theta \sin\theta \int_0^{2\pi} d\phi f(q, \theta, \phi), \quad (4)$$

where, in spherical coordinates $q_x = q \cos\phi \sin\theta$, $q_y = q \sin\phi \sin\theta$, $q_z = q \cos\theta$.

Another useful form of the scattering intensity, as a function of the correlation function, is the following [21]:

$$I(q) = 4\pi \int_0^D \gamma(r) \frac{\sin qr}{qr} r^2 dr, \quad (5)$$

where $\gamma(r) \equiv \langle \rho(\mathbf{r}) * \rho(-\mathbf{r}) \rangle$ is the correlation function of the object, with $\gamma(r) = 0$ for $r > D$ and D is the largest dimension in the object. The symbol $*$ denotes a convolution, and thus, the correlation function can be seen as an averaged self-convolution of density distribution.

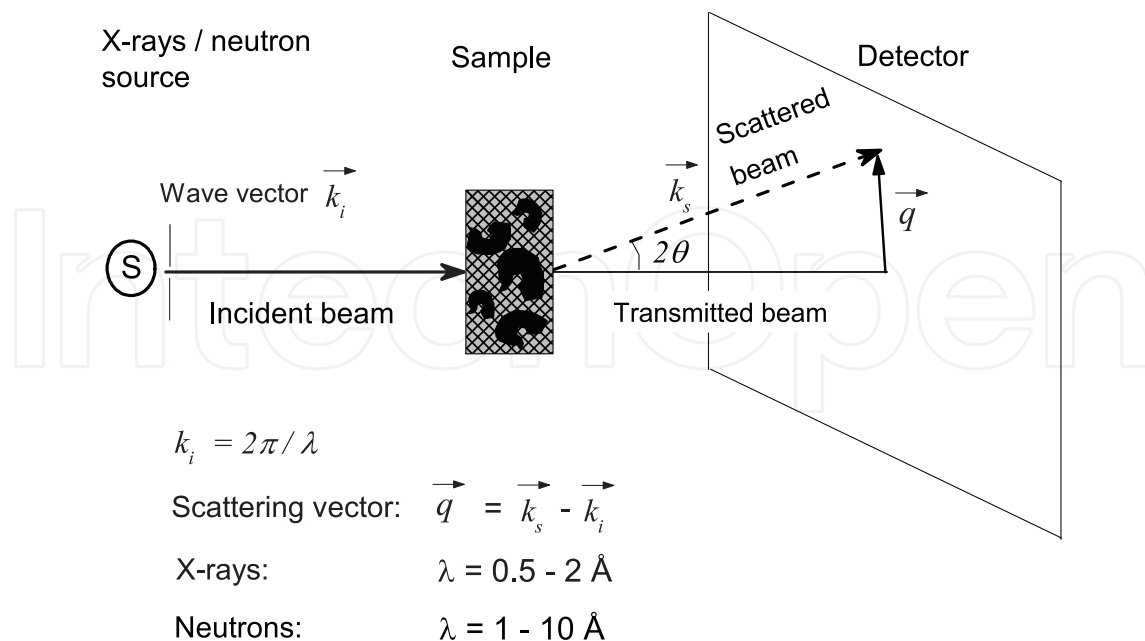


Figure 1. Schematic representation of a small-angle scattering experiment. 2θ is the scattering angle and λ is the wavelength of incident beam. The sample shown is a two-phase system of polydisperse scatterers with the same shape and random orientations, embedded in a matrix or solution.

At low values of the scattering vector ($q \lesssim 2\pi/D$), the above expression can be further exploited. By considering first the MacLaurin series

$$\frac{\sin(qr)}{qr} \simeq 1 - \frac{q^2 r^2}{6} + \frac{q^4 r^4}{120} - \dots, \quad (6)$$

and then using only the first two terms of this approximation into Eq. (5), the Guinier equation is obtained:

$$I(q) = I(0) \left(1 - \frac{q^2 R_g^2}{3} + \dots \right), \quad (7)$$

where $I(0) = 4\pi \int_0^D \gamma(r)r^2 dr$, and

$$R_g = \frac{1}{2} \int_0^D \gamma(r)r^4 dr / \int_0^D \gamma(r)r^2 dr, \quad (8)$$

is the radius of gyration of the object. In practice, a plot of $\log I(q)$ vs. q^2 is used to obtain the slope $R_g^2/3$, and then an overall size of the object. For a ball of radius R , it is known that $R = R_g \sqrt{5/3}$ [21]. If a scattering experiment is performed on an absolute scale, molecular weight can also be obtained.

However, as we shall see in the next sections, inside a fractal, the scattering units have defined positions and correlations, and the interference among rays scattered by different units may no longer be ignored, so that the scattering amplitudes of individual units have to be added. By considering that the fractal is composed of N balls of size R , its form factor becomes [29]:

$$F(\mathbf{q}) = \rho_q F_0(qR)/N, \quad (9)$$

where $\rho_q = \sum_j e^{-i\mathbf{q} \cdot \mathbf{r}_j}$ is the Fourier component of the density of units centers, F_0 is the form factor of each scattering unit composing the fractal, and \mathbf{r}_j are their positions. By introducing Eq. (9) into Eq. (2), the scattering intensity can be written as [29]:

$$I(q) = I(0) S(q) |F_0(qR)|^2 / N, \quad (10)$$

where $I(0) = n |\Delta\rho|^2 V^2$, and $S(q) \equiv \langle \rho_q \rho_{-q} \rangle / N$ is the structure factor and it describes the correlations between the scattering units inside the fractal.

A physical sample almost always consists of fractals that have different sizes, which is called polydispersity. An exception to this rule is protein solutions, in which all have the same size and shape. Thus, the corresponding scattering intensity from polydisperse fractals can be regarded as the sum of each individual form factor weighted with the corresponding volume V and contrast $\Delta\rho$. We consider here a continuous distribution $D_N(l)$ of fractals with different sizes l , defined in such a way that $D_N(l)dl$ gives the probability of finding a fractal with

dimension l lying in the range $(l, l + dl)$. Although any kind of broad distribution can be used, we take here, as an application, a log-normal distribution of fractal sizes, such as:

$$D_N(l) = \frac{1}{\sigma l (2\pi)^{1/2}} e^{-\frac{(\log(l/\mu_0) + \sigma^2/2)^2}{2\sigma^2}}, \quad (11)$$

where $\sigma = (\log(1 + \sigma_r^2))^{1/2}$, $\mu_0 = \langle l \rangle_D$ is the mean length, $\sigma_r = (\langle l^2 \rangle - \mu_0^2)^{1/2} / \mu_0$ is the relative variance, and $\langle \dots \rangle_D = \int_0^\infty \dots D_N(l) dl$. Since for a polydisperse fractal dispersion, the volume of each fractal has a continuous variation with its size, the polydisperse scattering intensity becomes:

$$I(q) = n |\Delta\rho|^2 \int_0^\infty \langle |F(\mathbf{q})|^2 \rangle V^2(l) D_N(l) dl, \quad (12)$$

where the form factor $F(\mathbf{q})$ is given by Eq. (9). The effect of polydispersity is to smooth the scattering curves [20, 21] (see also **Figure 2a**).

2.1.2. Debye-Pantos formula

In the next section, we shall make use of chaos game representation (CGR) and cellular automata (CA) to generate positions of the N scattering units/points. Thus, we can start with the Debye formula [44]

$$I^D(q) = NI_s(q) + 2F_s(q)^2 \sum_{i=1}^{N-1} \sum_{j=i+1}^N \frac{\sin qr_{ij}}{qr_{ij}}, \quad (13)$$

where $I_s(q)$ is the intensity scattered by each fractal unit, and r_{ij} is the distance between units i and j . When the number of units exceeds few thousands, the computation of the term $\sin(qr_{ij})/(qr_{ij})$ is time consuming, and thus it is handled via a pair-distance histogram $g(r)$, with a bin-width commensurate with the experimental resolution [45]. Thus, Eq. (13) becomes

$$I^D(q) = NI_s(q) + 2F_s^2(q) \sum_{i=1}^{N_{\text{bins}}} g(r_i) \frac{\sin qr_i}{qr_i}, \quad (14)$$

where $g(r_i)$ is the pair-distance histogram at pair distance r_i . For determining fractal properties, we can neglect the form factor, and consider $I_s(q) = F_s^2(q) = 1$. Thus, Eq. (14) gives the structure factor:

$$I^D(q) \equiv S^D(q) = N + 2 \sum_{i=1}^{N_{\text{bins}}} g(r_i) \frac{\sin qr_i}{qr_i}. \quad (15)$$

2.1.3. Scattering from a ball and from a triangle

As a first example, we derive the scattering intensity of a ball with unit density, radius R , and volume $V = (4\pi/3)R^3$. To do so, we can rewrite the normalized scattering amplitude given by Eq. (3), in spherical coordinates, such as:

$$F_0(\mathbf{q}) = \frac{1}{V} \int_{\phi=0}^{2\pi} \int_{\theta=0}^{\pi} \int_{r=0}^{\infty} e^{-i\mathbf{q} \cdot \mathbf{r}} r^2 \sin \theta dr d\theta d\phi. \quad (16)$$

Note that since balls represent here the basic units of the fractal, we have chosen the notation $F_0(\mathbf{q})$ instead of $F(\mathbf{q})$, in spirit of Eq. (9). We can choose the polar axis to coincide with the direction of \mathbf{q} , and therefore $\mathbf{q} \cdot \mathbf{r} = qr \cos \theta$. By denoting $u = \cos \theta$, in the new variable, Eq. (16) becomes:

$$F_0(\mathbf{q}) \equiv \frac{1}{V} \int_{\phi=0}^{2\pi} \int_{u=-1}^1 \int_{r=0}^{\infty} e^{-iqr u} r^2 \sin \theta dr d\theta d\phi = \frac{1}{V} \int_{r=0}^R 4\pi r^2 \frac{\sin(qr)}{qr} dr. \quad (17)$$

By performing an integration by parts of the last expression, the normalized scattering amplitude of the ball of radius R becomes:

$$F_0(qR) = \frac{3(\sin(qR) - (qR) \cos(qR))}{(qR)^3}. \quad (18)$$

Thus, the total scattering intensity (see also Eq. (2)) becomes:

$$I(q) \equiv [F_0(qR)]^2 = \frac{3^2(\sin(qR) - (qR) \cos(qR))^2}{(qR)^6}. \quad (19)$$

Figure 2a shows the scattering intensity of a ball of radius $R = 10$ nm. The scattering is represented on a double logarithmic scale and shows the presence of two main regions. At low values of the scattering vector ($q \lesssim \pi/R$), we have the Guinier region, which is a plateau with $I(q) \propto q^0$, and from which one can obtain the radius of gyration, as described in the previous section. At higher values (i.e., $q \gtrsim \pi/R$), there is a power-law decay of the type $I(q) \propto q^{-4}$ and with many minima. This is called the Porod region and generally it gives information about the specific surface of the investigated object. The main feature here is that by increasing the relative variance σ_v the scattering curve

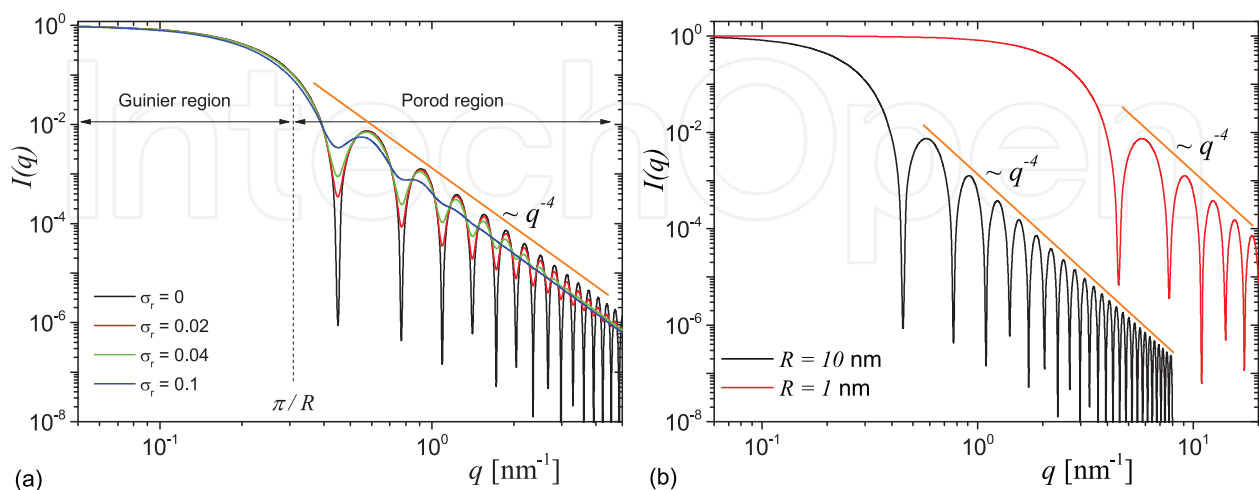


Figure 2. (a) SAS intensity from a ball of radius $R = 10$ nm from Eq. (19) (lowest curve). The higher the relative variance, the smoother the curve. Polydisperse SAS intensity, according to Eq. (12) at various values of relative variances. (b) SAS intensities from a ball of radius $R = 10$ nm (left curve), and $R = 1$ nm (right curve).

becomes smoother, and the value of the scattering exponent is preserved. **Figure 2b** shows that by decreasing the size of the ball, the corresponding scattering curve has the same characteristics and the Porod region is shifted to the right with the corresponding factor (here by 10).

The second example is an equilateral triangle of edge size a . This is a slightly more complicated structure since it does not have a center of symmetry as a ball, and thus an orientational averaging is required. Thus, its height is $h = a\sqrt{3}/2$ and its surface area is:

$$Area(a) = a^2 \frac{\sqrt{3}}{4}. \quad (20)$$

We choose a Cartesian coordinate system where one edge is parallel to the x-axis and the opposite vertex coincides with the origin. Thus, Eq. (3) becomes a surface integral given by:

$$F_0(\mathbf{q}) = \frac{1}{Area(a)} \int_0^a dy \int_{-\frac{ya}{2h}}^{\frac{ya}{2h}} dx e^{-i(xq_x + yq_y)}, \quad (21)$$

which can be calculated and transformed into:

$$F_0(\mathbf{q}) = 2e^{-i\alpha} \frac{\beta e^{i\alpha} - \beta \cos \beta - i\alpha \sin \beta}{\beta(\beta^2 - \alpha^2)}, \quad (22)$$

where $\alpha = hq_x$ and $\beta = hq_y$. As we shall see in next sections, the scattering amplitude of a system of triangles can be obtained by properly taking into account their scaling, rotation, and translations.

The averaging over all orientations is performed by allowing the triangle to rotate in a 2D space, and thus the average given by Eq. (4) for 3D case, becomes now:

$$\langle f(q_x, q_y) \rangle = \frac{1}{2\pi} \int_0^{2\pi} d\phi f(q, \phi), \quad (23)$$

with $q_x = q \cos \phi$ and $q_y = q \sin \phi$.

Similarly to scattering from a ball, the intensity curve of a triangle also shows the Guinier region at low- q ($q \lesssim 2\pi/a$), and a Porod region at high- q ($q \gtrsim 2\pi/a$) as shown in **Figure 3a**. However, for a triangle, the absolute value of the scattering exponent in the Porod region is equal to 3. This is in contrast to the value of 4 obtained for the ball in the previous example (see **Figure 3b**). The difference arises due to the fact that the triangle is a 2D object while the ball is a 3D one. In addition, due to the lack of symmetry, scattering from a triangle does not show pronounced minima as in the case of scattering from a ball.

2.1.4. Scattering from systems of triangles

In the previous section, we have seen that regardless of the shape and Euclidean dimension, the SAS intensity from basic geometrical structures always reproduces a Guinier region followed by a Porod one. Without losing from generality, we will restrict in the following to calculate SAS intensity from systems of triangles. In principle, any geometrical shape can be chosen but we

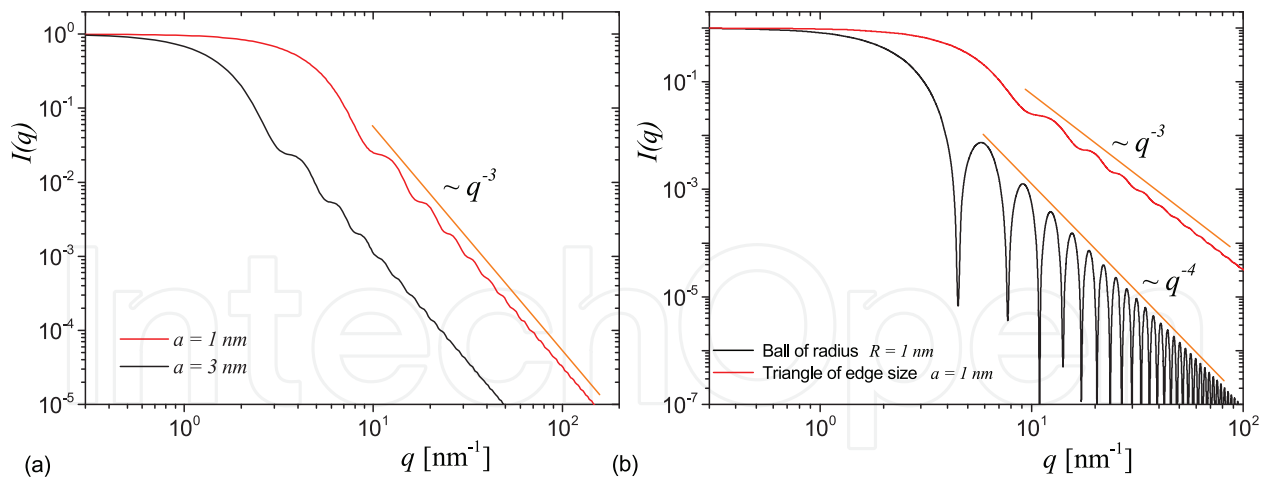


Figure 3. (a) SAS intensity from an equilateral triangle of edge size $a = 1$ nm (right curve), and $a = 3$ nm (left curve), respectively. (b) A comparison between the SAS intensity of a ball of radius $R = 1$ nm (left curve) and a triangle of edge size $a = 1$ nm (right curve).

prefer here triangles due to the fact that the both well-known techniques for generating fractal structures: iteration function systems and cellular automata, in their basic form, involve triangles in the construction process.

We start first with a simple model consisting of three triangles of edge size $a/2$, with $a = 1$ nm, as shown in **Figure 4a**. For this configuration, we can write [40]:

$$Area(a/3)F(\mathbf{q}) = \sum_{j=0}^2 \beta_s^2 Area(a)F_0(\beta_s \mathbf{q})e^{-i\mathbf{q}\mathbf{a}_j}, \quad (24)$$

where β_s is the scaling factor, $F_0(\mathbf{q})$ is given by Eq. (22), and the translation vectors are given by:

$$\mathbf{a}_j = \frac{a\sqrt{3}}{6} \left\{ \cos \frac{\pi}{3} \left(2j + \frac{3}{2} \right), \sin \frac{\pi}{3} \left(2j + \frac{3}{2} \right) \right\} \quad (25)$$

The corresponding scattering intensity is shown in **Figure 4b**, and as expected, it consists of a Guinier region followed by a Porod one with scattering exponent -3 . For comparison, the same figure shows the scattering intensity of a single of edge size $a = 1$ nm.

The second example is a system of 6 triangles of edge sizes $a/3$ arranged in such a way that they form a hexagon as shown in **Figure 5a** in black. For this configuration, the translation vectors can be written as [38]:

$$\mathbf{b}_j = \frac{2a}{3\sqrt{3}} \left\{ \cos \frac{\pi}{3} j, \sin \frac{\pi}{3} j \right\}. \quad (26)$$

The corresponding scattering intensity is shown in **Figure 5b** and shows a superposition of maxima and minima. Excepting the distribution of minima in the Porod region, there is no significant difference between this scattering curve and the one corresponding to the system of three triangles shown in **Figure 4b**.

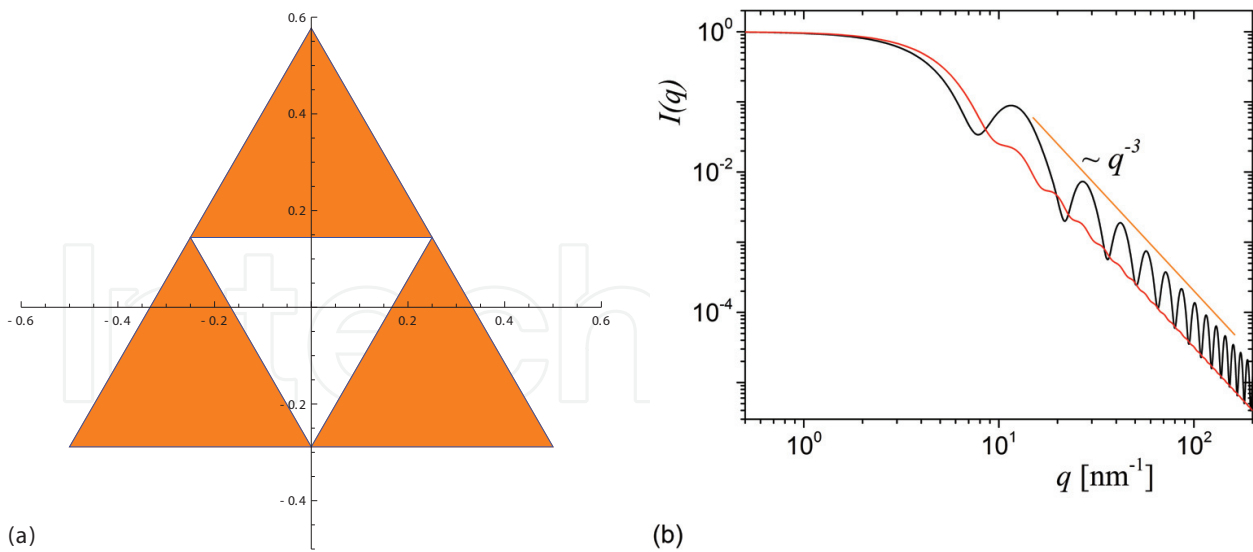


Figure 4. (a) A model of three triangles (gray) of edge size $a/2$, with $a = 1$ nm; (b) the corresponding SAS intensity (highly oscillating curve). The smoother curve is the SAS intensity corresponding to a single triangle of edge size $a = 1$ nm and whose center coincides with the center of white triangle in part (a).

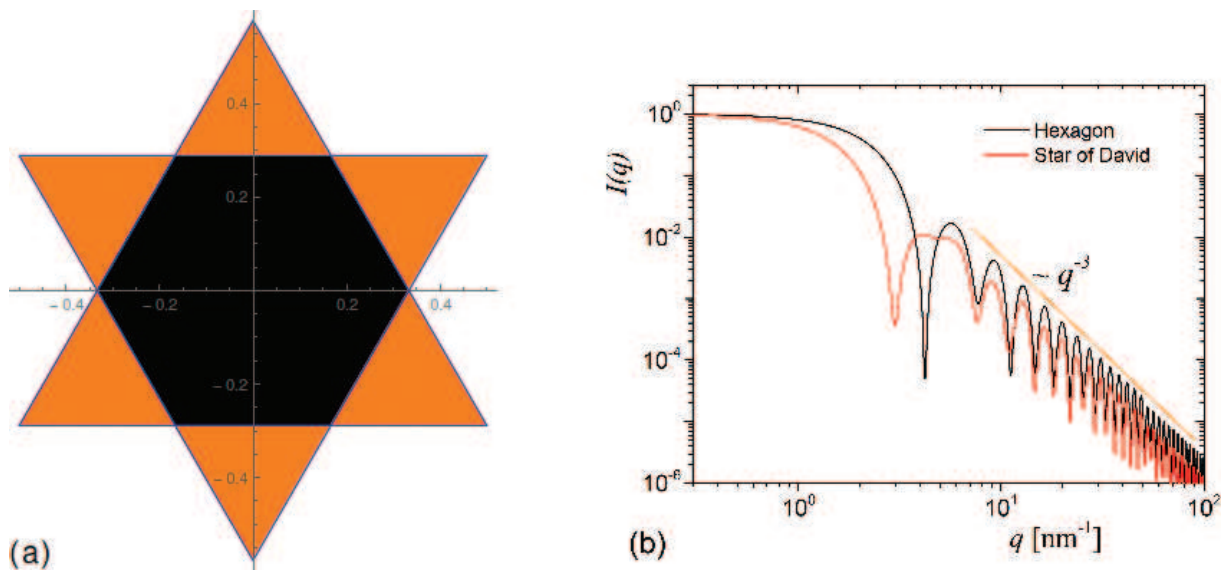


Figure 5. (a) Two models consisting only of equilateral triangles: hexagon (black color) and Star of David (black and gray colors); (b) the corresponding SAS intensities of the hexagon (continuous curve) and Star of David (dashed curve).

The last example is slightly more complicated and it consists of one hexagon of edge size $a/3$ (black) and six triangles of edge size $a/3$ (gray), with $a = 1$ nm arranged as in **Figure 5a**. This configuration is equivalent to a system of one triangle of edge size a and three triangles of edge size $a/3$. This is known in the literature, also as the Star of David. The translation vectors of the three triangles can be obtained in a similar way, as in the case of the first example. The corresponding scattering intensity is shown in **Figure 5b** (red). It can be seen that due to various sizes of the triangles involved in the construction, an intermediate regime emerges between the Guinier and Porod regions, approximately at $2 \lesssim q \lesssim 8 \text{ nm}^{-1}$. As we shall see later, for even more complex structures, this intermediate region will evolve into a fractal one.

In particular, if the triangles composing the system are arranged in such a way that they form a Sierpinski gasket, the intermediate region will correspond to a mass fractal region [29–31]. When the triangles have a power-law distribution in their sizes, the intermediate region will correspond to a surface fractal one [37, 38]. The great advantage of the SAS technique consists in the possibility to differentiate these two types of fractal regimes, as discussed at the beginning of this chapter.

2.2. Mass and surface fractals

As it was already pointed out before, the main characteristic of fractals obtained from a SAS experiment is the fractal dimension. Mathematically, the α -dimensional Hausdorff measure is defined by [29]

$$m^\alpha(A) = \liminf_{a \rightarrow 0} \sum_{\{V_i\}} a_i^\alpha, \alpha > 0 \quad (27)$$

where A is a subset of an n -dimensional Euclidean space, $\{V_i\}$ is a covering of A with $a_i = \text{diam}(V_i) \leq a$, and the infimum is on all possible coverings. Then, the Hausdorff dimension D of the set A is given by:

$$D \equiv \inf\{\alpha_i, m^\alpha(A) = 0\} = \sup\{\alpha, m^\alpha(A) = \infty\}, \quad (28)$$

and it represents the value of α for which the Hausdorff measure changes its value from zero to infinity.

However, in practice, this definition is quite inconvenient to be used, and here we shall use the “mass-radius” relation for calculating the Hausdorff dimension of the fractals [1]. In this approach, the total fractal measure (i.e., mass, surface area, volume) of the fractal within a ball of radius r centered on the fractal is given by:

$$M(r) = A(r)r^D, \quad (29)$$

where $\log A(r)/\log r \rightarrow 0$ for $r \rightarrow \infty$.

As an application, for a deterministic mass fractal of length L , scaling factor β_s , and k structural units in the first iteration, we can write [1]:

$$M(L) = kM(\beta_s L), \quad (30)$$

and using Eq. (29), one obtains a formula for calculating the fractal dimension of the mass fractal:

$$k\beta_s^D = 1. \quad (31)$$

Thus, if a finite iteration of the fractal consists of N scattering balls of radius a , the fractal dimension is given by the asymptotic:

$$N \propto \left(\frac{L}{a}\right)^D, \quad (32)$$

in the limit of large number of iterations.

If the quantity to be measured is the *mass* $M(r)$ embedded in a disk of radius r , Eq. (30) becomes $M(r) \propto r^{D_m}$, which leads to $I(q) \propto q^{-D_m}$. The lower the value of mass fractal dimension D_m , the less compact is the structure. In a similar way, for a surface fractal of fractal dimension D_s , its surface obeys $S(r) \propto r^{2-D_s}$ and thus the scattering intensity decays as $I(q) \propto q^{-(2d-D_s)}$.

More generally, in a two-phase system where one phase is of dimension D_m and the second phase is its complement set of dimension D_p ("pores"), the "boundary" between the two phases also forms a set of dimension D_s ("surface"). Thus, for a mass fractal, we have $D_s = D_m < d$ and $D_p = d$, while for a surface fractal we have $D_m = D_p = d$ and $d - 1 < D_s < d$ [37, 38]. The possibility of differentiating between mass and surface fractals makes SAS a very convenient technique for measuring fractal dimensions of materials at nano- and micro-scales.

2.3. Iterated function system

As a first method of generating fractals, we consider an iterated function system (IFS). By definition, an IFS is a complete metric space (X, d) together with a finite set $w_n: X \rightarrow X$ of contraction mappings and contractivity factors $s_n, n = 1, 2, \dots, N$. In general, a transformation $f: X \rightarrow X$ on a metric space (X, d) is a contraction mapping if there is a constant (contractivity factor) $0 \leq s < 1$ such that

$$d(f(x), f(y)) \leq s \cdot d(x, y) \quad \forall x, y \in X. \quad (33)$$

By considering a hyperbolic IFS and if we denote by $(H(X), h(d))$, the space of nonempty compact subsets with the Hausdorff metric $h(d)$, then the transformations $W: H(X) \rightarrow H(X)$ defined by $W(B) = \cup_{n=1}^N w_n(B), \forall B \in H(X)$ is a contraction mapping on the complete metric space $(\mathcal{H}(X), h(d))$ with the contractivity factor s [46], i.e.,

$$h(W(B), W(C)) \leq s \cdot h(B, C) \quad \forall B, C \in \mathcal{H}(X). \quad (34)$$

The unique fix point $A \in \mathcal{H}(X)$ obeys $A = \cup_{n=1}^N w_n(A)$ and is called the attractor of the IFS, which is a deterministic fractal [46].

We generate here the attractor by using random iteration algorithm, and thus we assign the probability $p_n > 0$ to w_n for $n = 1, 2, \dots$ where $\sum_{n=1}^N p_n = 1$. Then, a point $x_0 \in X$ is chosen, and we build recursively the sequence $x_k \in \{w_1(x_{k-1}), w_2(x_{k-1}), \dots, w_N(x_{k-1})\}$, where the probability of the event $x_k = w_n(x_{k-1})$ is p_n , and $k = 1, 2, \dots$. This leads to the sequence $\{x_{k-1} : k = 0, 1, \dots\}$, which converges to the attractor of IFS.

2.4. Cellular automata

Another important method to generate exact self-similar fractals is by using cellular automata (CA) [47–49]. They provide simple models for dynamical systems dealing with the emergence of collective phenomena such as chaos, turbulence, or fractals. Basically, a cellular automaton is a set of cells on a grid (rectangular, hexagonal, etc.) that evolves through a number of discrete steps according to a set of rules based on the states of neighboring cells. The rules are then

applied alternatively for as many times as needed. The grid is n -dimensional but for our purposes, we will choose $n = 1$.

In this chapter, we shall present Rule 90 [49] together with the corresponding structure factor based on Pantos formula given by Eq. (15). For particular values of the number of steps, Rule 90 generates exact shapes of the Sierpinski gasket (SG). However, for most of the number of steps, it generates intermediate structures between two consecutive iterations of SG. Thus, for Rule 90, CA extends considerably the number of structures generated, and therefore new classes of materials consisting of a “mixture” of SG at various iterations can be investigated.

More generally, SAS from CA could be used to check whether a generated structure is a mass or surface fractal (or none of them), i.e., whether there exists a power-law distribution of some entities (collections of cells). In addition, through the oscillations of the scattering curve in the fractal region, SAS from CA can shed some light on the randomness of the generated structures. This could be of particular interest since some rules like Rule 30 generates so-called pseudo-random structures. However, this is beyond the scope of this chapter. Here, we shall restrict ourselves to calculation and interpretation of SAS intensities from basic structures, such as those based on SG. This shall facilitate a quick comparison with the theoretical model based on SG presented in the next section, and thus to support the validity of the obtained results.

3. Small-angle scattering from mass fractals

As an example of a deterministic mass fractal, we calculate the scattering from a two dimensional Sierpinski gasket (SG), generated by three different methods. In order to calculate the scattering intensities of an ensemble of triangles, we use the following properties:

- When the size of a triangle is scaled as $a \rightarrow \beta_s a$, then the form factor scales as $F(\mathbf{q}) \rightarrow F(\beta_s \mathbf{q})$;
- When the triangle is translated by a vector \mathbf{b} such as $\mathbf{r} \rightarrow \mathbf{r} + \mathbf{r}$, then $F(\mathbf{q}) \rightarrow F(\mathbf{q})e^{-i\mathbf{q} \cdot \mathbf{b}}$.

Zero-th iteration of SG consists of a single triangle of edge size a (here, $a = 1$ nm). First iteration ($m = 1$) consists of four smaller triangles, each of the edge length $a/2$ as shown in **Figure 3a**. At second iteration ($m = 2$), the same operation is repeated for each of the triangles of edge length $a/2$. In the limit of large number of iterations m , the total number of triangles of edge size $a_m = a/2^m$ is:

$$N = 3^m. \tag{35}$$

Therefore using Eq. (31), one obtains the fractal dimension of SG as:

$$D = \lim_{m \rightarrow \infty} \frac{\log N}{\log (a/a_m)} \approx 1.585. \tag{36}$$

At m -th iteration, the positions of the triangles forming the SG are given by:

$$P_m(\vec{q}) \equiv \prod_{i=1}^m G_i(\vec{q}), \quad (37)$$

where $G_i(\vec{q})$ is known as the generative function [29, 31, 38], and is given by

$$G_1(\vec{q}) = \frac{1}{3} \sum_{j=0}^2 e^{-i\vec{q} \cdot \vec{a}_j}, \quad (38)$$

where the translation vectors are given by Eq. (25), $G_m(\vec{q}) = G_1(\beta_s^{m-1} \vec{q})$, and $\beta_s = 1/2$. **Figure 5** left part, shows first three iterations of SG.

By using the property given in Eq. (37), the fractal structure factor can be written as [29]:

$$S(q)/N = \left\langle \prod_{i=1}^m |G_i(\vec{q})|^2 \right\rangle \quad (39)$$

Thus, by introducing Eqs. (39) and (22) into Eq. (10), we obtain an analytical expression for the scattering intensity:

$$I(q)/I(0) = \left\langle |F_0(\beta_s^m a \vec{q})|^2 \right\rangle S(q)/N. \quad (40)$$

By ignoring the form factor F_0 in Eq. (40), an analytical expression of the structure factor is obtained. This case is discussed in [40].

The corresponding scattering intensities are shown in **Figure 5** right part, for a triangle ($m=0$) and for the first three iterations of SG ($m=1, 2, 3$). At low q -values ($q \lesssim 2 \text{ nm}^{-1}$), all the scattering curves are characterized by a Guinier region. A main feature of scattering from deterministic mass fractals is that after the Guinier region, it follows a fractal regime in which the absolute value of the scattering exponent equals the fractal dimension of the fractal. The length of the fractal regime increases with increasing the iteration number since the distances between the scattering units of the fractals (here triangles) decrease. In **Figure 5** right part, the fractal regime is clearly seen within the range $2 \lesssim q \lesssim 14 \text{ nm}^{-1}$ for $m=3$. It is characterized by a succession of maxima and minima superimposed on a power-law decay (also known as a generalized power-law decay [29]). The number of minima in the fractal regime is equal with the fractal iteration number and from their periodicity, we can extract the value of the scaling factor [29]. Beyond the fractal regime, one obtain as expected, the Porod region where the exponent of the power-law decay is -3 (or -4 for three-dimensional objects). In **Figure 5** right part, at $m=3$ the Porod regime begins near $q \gtrsim 14 \text{ nm}^{-1}$.

By taking into account, the effect of polydispersity or the random distribution of the scattering units, the scattering curve is smoothed and thus the maxima and minima are smeared out. The "smoothness" of the curve increases with increasing the relative variance of the distribution function, and they can be completely smeared out when a threshold is reached. Experimentally,

most of the times, SAS experiments give this type of behavior, when the curve is completely smeared out. Please note that if we neglect the contribution of the form factor F_0 in Eq. (40), then the Porod region is replaced by an asymptotic region, from which the number of scattering units inside the fractal can be obtained (see **Figure 6**). This case is presented and discussed in the following, for the SG generated using CGR and IFS, respectively.

CGR representation gives directly the positions of the scattering units in the fractal. **Figure 6** left part, shows the SG generated from CGR for $N=30, 130, 230$, and for 430 points, respectively. The figure clearly shows that by increasing the number of points, the obtained structure approaches better the structure of SG. From the same figure, we can see that for $N=430$ points, the second iteration of SG can be quite clearly distinguished. Thus, a convenient way to calculate the scattering intensity is to use Pantos formula given by Eq. (15), since we neglect the shape of the scattering units.

Figure 6 right part shows the scattering structure factor of SG built from the CGR, for the four structures in the left part. Generally, all scattering curves are characterized by the presence of the three main regions specific to SG, obtained using the analytic representation (**Figure 5**) right part: Guinier region at low q , fractal region at intermediate q , and here an asymptotic region instead of a Porod one, since we neglect the form factor. The same figure shows that by increasing the number of particles, the length of the fractal region also increases. This is to be expected, since increasing the number of points leads to a better approximation of the deterministic SG. However, for SG generated using CGR, a transition region appears (at $40 \lesssim q \lesssim 200$), since in this region, the pair distance distribution function does not follow a power-law decay distribution of the number of distances. Finally, in the asymptotic region, the curves are proportional to $1/N$, and thus, the number of points can be recovered. The asymptotic values of the curves are marked by horizontal dashes lines in **Figure 5** right part.

Rule 90 (**Figure 7** left part) is an elementary cellular automaton rule, and it produces SG for particular values of the number of steps. Although the system is generated on a rectangular

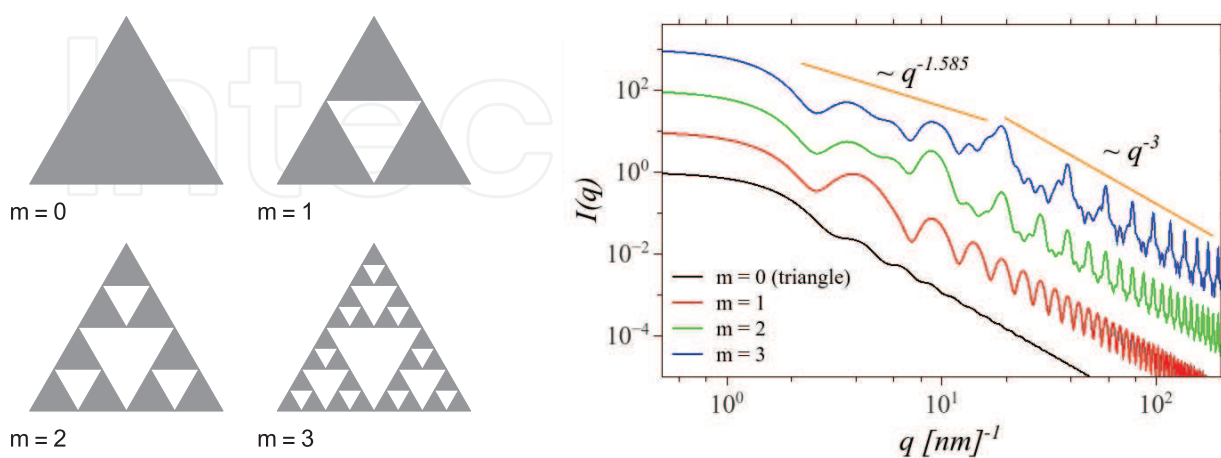


Figure 6. Left part: first four iterations of the Sierpinski gasket generated using a deterministic algorithm; right part: The corresponding SAS intensities of the Sierpinski gasket. The curves are shifted vertically by a factor 10^m , for clarity. The lowest curve corresponds to $m=0$, and the highest one corresponds to $m=3$.

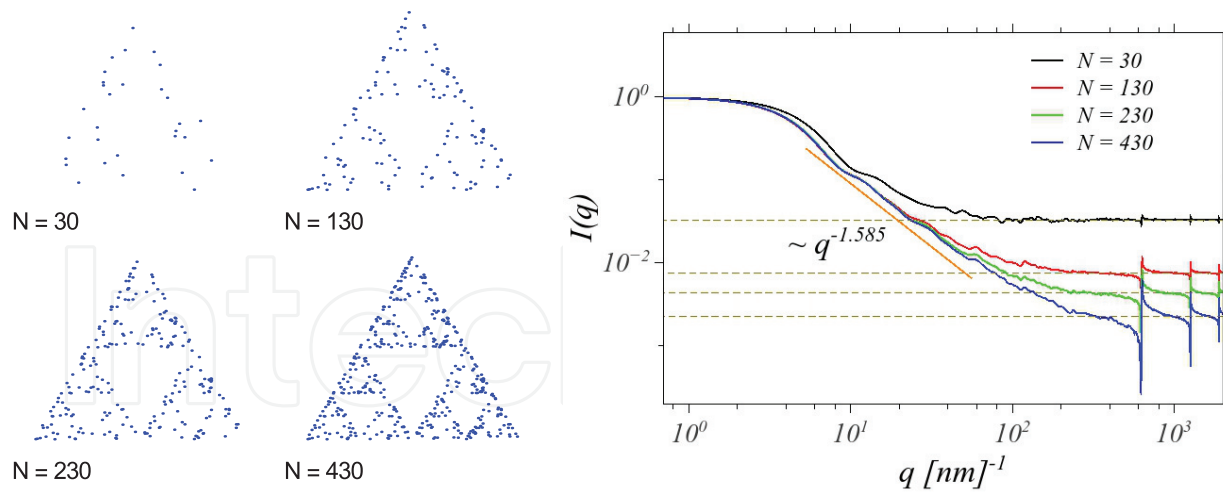


Figure 7. Left part: Sierpinski gasket generated using CGR, for different values of the number of scattering units; right part: the corresponding SAS intensities of the Sierpinski gasket from CGR. The highest curve corresponds to $N = 30$ and the lowest one corresponds to $N = 430$.

grid with cells of finite size, we consider here (as in the previous example) that the scattering units are points centered in the cells. **Figure 7** left part, shows the structure generated by Rule 90 for $p=31, 41, 51$, and for $p=63$ steps, respectively. Note that $p=31$ and $p=63$ correspond to SG at iterations $m=3$, and $m=4$, respectively, while $p=41$ and $p=52$ correspond to some intermediate structures between the two consecutive iterations.

The corresponding structure factors are shown in **Figure 7** right part. In the scattering curve, all the three main regions are present: Guinier, fractal, and asymptotic regions. However, as opposed to the Guinier region of the SG generated deterministically, or through CGR, here its length decreases with increasing the number of steps. This is a consequence of the construction algorithm used, namely the structure increases its size at every step. Decreasing the length of the Guinier region leads to an increase of the fractal one, since the smallest distances between scattering points remain the same. This is indicated in the scattering curve, by approximately equal positions ($q \approx 360 \text{ nm}^{-1}$) of the first minima, for each of the four steps. As expected, the absolute value of the scattering exponent in the fractal region coincides with the fractal dimension of the structure, and the asymptotic behavior at large q (shown by horizontal dotted lines in **Figure 7** right part) tends to $1/N$, where N is the total number of scattering points.

4. Small-angle scattering from surface fractals

Recently, it has been shown that surface fractals can be built as a sum of mass fractals [37, 38]. As an example, we consider here a generalized version of the Koch snowflake (KS). The construction algorithm starts from an equilateral triangle with edge length a , which is the zero-th mass fractal iteration (black triangle in **Figure 8** left part). At the second step, each side is divided into three segments, each of length $a/3$, and a new triangle pointing outward is added. The base of the new triangle coincides with the central segment. This is the first mass fractal iteration (three

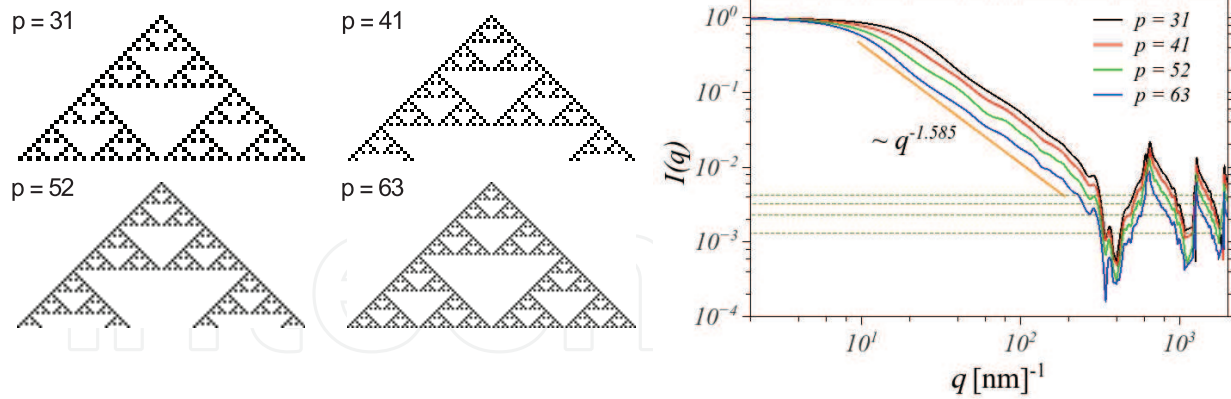


Figure 8. Left part: Rule 90 for $p=31, 41, 52$ and $p=63$ number of steps, respectively; right part: the corresponding scattering intensities. The leftmost curve corresponds to $p=63$ and the rightmost one corresponds to $p=31$.

orange triangles in **Figure 8** left part). By repeating the same procedure for each of the new triangles, one obtains the KS having the fractal dimension:

$$D_s = \lim_{m \rightarrow \infty} \frac{\log 3 \cdot 4^m}{\log (a/a_m)} = \frac{\log 4}{\log 3} \approx 1.26, \quad (41)$$

where a_m is the side length at m th iteration. In **Figure 8**, each of the triangle is scaled down by a factor of $0.6 \cdot a_m$. The case when the triangles are not scaled down corresponds exactly to the well-known KS and its scattering properties have been extensively studied in [38].

Since a surface fractal can be constructed as a sum of mass fractals, the normalized scattering amplitude is written as a sum of the scattering amplitudes of mass fractals. If we denote $A_m(\vec{q}) \equiv \text{Area}(a)F_m(\vec{q})$, then a recurrence formula for the scattering amplitude of the surface fractal at arbitrarily iteration can be written as [38]:

$$A_m(\vec{q}) = 6G_3(\vec{q}) \left[\beta_s^2 A_{m-1}(\beta_s \vec{q}) - 6G_2(\beta_s \vec{q}) \beta_s^4 A_{m-2}(\beta_s^2 \vec{q}) \right] + \beta_s^2 A_{m-1}(\beta_s \vec{q}) \left[1 + 6G_2(\vec{q}) \right]. \quad (42)$$

Here, the scaling factor is $\beta_s=3/10$, and the generative functions are given by:

$$G_2(\vec{q}) = \frac{1}{6} \sum_{j=0}^5 e^{-i\vec{q} \cdot \vec{c}_j}, \quad (43)$$

and respectively by:

$$G_3(\vec{q}) = \frac{1}{6} \sum_{j=0}^5 e^{-i\vec{q} \cdot \vec{b}_j}. \quad (44)$$

The translation vectors are defined as:

$$\vec{c}_j = \frac{2a}{9} \{ \cos \pi(j + 1/2)/3, \sin \pi(j + 1/2)/3 \}, \quad (45)$$

and the vectors \vec{b}_j are given by Eq. (26). Thus, using Eq. (2), the non-normalized scattering amplitude is $I(q) \propto \langle |A_m(\vec{q})|^2 \rangle$, provided the amplitudes at $m=0$ and $m=1$ are known.

Figures 8 and 9 left parts show the construction of the generalized KS when the ratio between the sizes of the triangles and the distances between them are 0.6 and 0.4, respectively. **Figures 8 and 9** right parts show the corresponding scattering intensities. The general feature is that when the ratio is 0.4, in the fractal region the overall agreement between the total scattering intensity and the intensity corresponding to uncorrelated triangles is slightly better. The curve also shows that the absolute value of the scattering exponent is now $6 - D_s$, with $D_s = 1.26$ given by Eq. (41), which is a “signature” of scattering from surface fractals. The reason for such behavior is that at a given iteration, the surface fractal consists of scattering units of different sizes following a power-law distribution (see **Figure 8** left part), while mass fractals consist of scattering units of the same size (see **Figure 5** left part). A mathematical derivation of the value of the scattering exponent in the case of scattering from surface fractals can be found in [37, 38].

The centers of triangles in **Figure 8** left part coincide with the centers of triangles of the regular KS. From another hand, it has been recently shown that the scattering intensity corresponding to a system of triangles whose sizes follow a power-law distribution and whose positions are uncorrelated, approximates under certain conditions the scattering intensity of the same system but when the positional correlations are not considered [38]. **Figure 8** right part, shows also the scattering intensity of a system of triangles whose positions are uncorrelated (red curve). We can observe that in the fractal region ($20 \lesssim q \lesssim 400 \text{ nm}^{-1}$), the approximation is not quite satisfactory. The reason of this behavior is that here the scaling factor is β_s , and thus the distances between the centers of the triangles is of the same order as their size. However, when the distances between

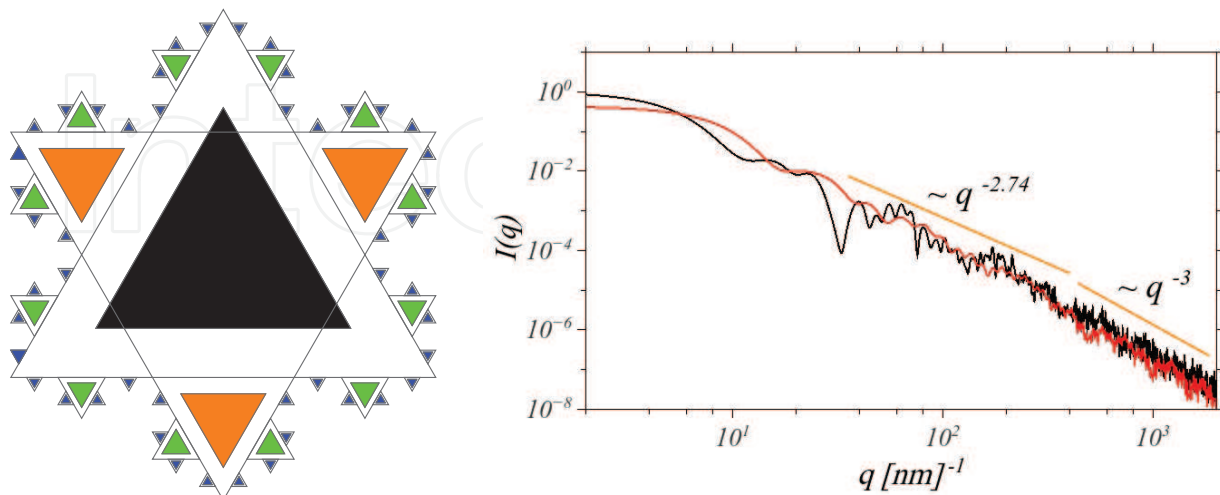


Figure 9. Left part: a generalized Koch snowflake model. Right part: highly oscillating curve—the corresponding scattering intensity, smoother curve—the scattering intensity from a system containing the same number of triangles but whose positions are randomly.

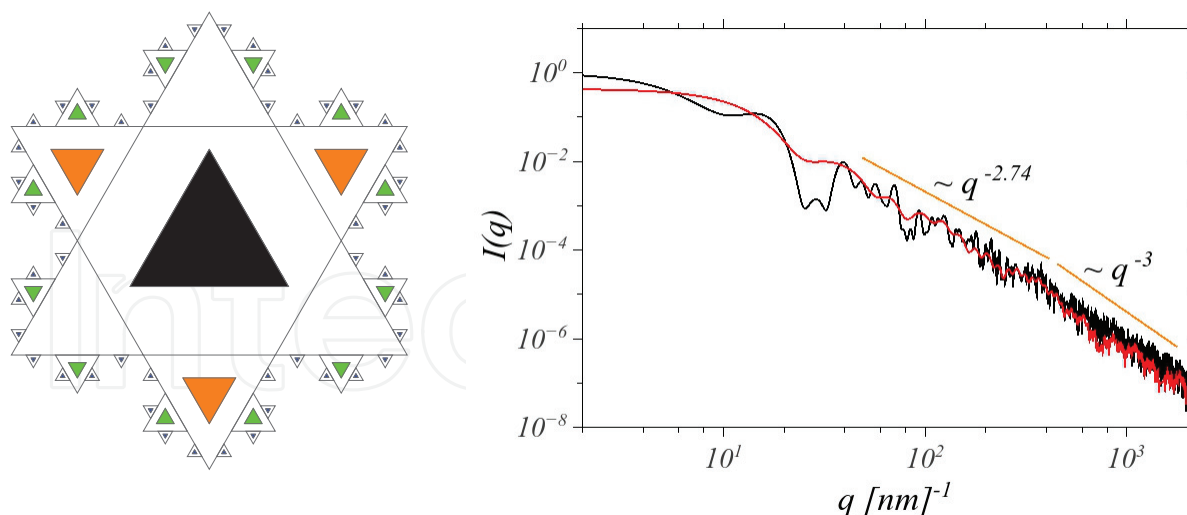


Figure 10. Left part: a generalized Koch snowflake model. Right part: highly oscillating curve—the total scattering intensity, smoother curve—the scattering intensity from a system containing the same number of triangles but whose positions are random.

the scattering units are much bigger than the sizes of the units, the approximation of the uncorrelated positions of the triangles works fairly well in the fractal region [38] (**Figure 10**).

5. Conclusions

In this chapter, we have presented and discussed some general concepts in small-angle scattering (SAS; neutrons, X-ray, light) from deterministic mass and surface fractals. To do so, we have considered the Sierpinski gasket (SG) as a model for deterministic mass fractals, and a generalized version of Koch snowflake (KS) as a model for deterministic surface fractals. The model for SG has been introduced through three main algorithms: deterministic and random iteration function system (IFS), and through cellular automata (CA). KS has been constructed in the framework of deterministic IFS.

The SAS intensities (fractal and structure factor) has been calculated from a system of 2D, monodisperse diluted (i.e., spatial correlation can be neglected) and randomly oriented fractals. They are characterized by the presence of three main regions: Guinier (at low q), fractal (at intermediate q), and Porod/asymptotic (at high q). We have shown that in the case of mass fractals, we can extract structural information about the fractal dimension (from the exponent of the SAS curve in the fractal region), scaling factor (from the periodicity of minima in the fractal region), iteration number (from the number of minima in the fractal region), and the total number of scattering units inside a fractal (from the value of the structure factor in the asymptotic region). In addition, mass fractals generated using IFS are able to reproduce fairly well the scattering curve of deterministic IFS under the proper conditions. Mass fractals generated from CA increase their size with increasing the number of steps. This growing process is also reflected by a decrease of the length of Guinier region. We have also shown that

a surface fractal can be considered as a superposition of mass fractals at various iterations and the range of structural information which can be extracted is similar to the case of scattering from mass fractals.

The IFS and CA algorithms used to generate the mass fractals models can be easily extended to more general structures and can be used to address various questions. For example, in the case of CA, SAS could be used to determine the fractal dimension of an arbitrary structure generated using one dimensional rules, it can shed some light on the randomness of some structures, or it can reveal the existence of a power-law distribution of some entities (of arbitrarily shape) generated by a specific rule.

Author details

Eugen Mircea Anitas^{1,2*}

*Address all correspondence to: anitas@jinr.ru

1 Joint Institute for Nuclear Research, Dubna, Moscow Region, Russian Federation

2 Horia Hulubei National Institute of Physics and Nuclear Engineering, Bucharest-Magurele, Romania

References

- [1] Mandelbrot BB. *The Fractal Geometry of Nature*. New York: W. H. Freeman; 1982. 468 p
- [2] Feder J. *Fractals*. New York: Springer; 1988. 284 p
- [3] Vicsek T. *Fractal Growth Phenomena*. 2nd ed. Singapore: World Scientific; 1992. 528 p
- [4] Bunde A, Havlin S, editors. *Fractals and Disordered Systems*. 2nd ed. Berlin Heidelberg: Springer; 1995. 408 p. DOI: 10.1007/978-3-642-84868-1
- [5] Willis BTM, Carlile CJ. *Experimental Neutron Scattering*. Great Britain: Oxford University Press; 2009. 344 p
- [6] Strangl J, Mocuta C, Chamard V, Carbone D. *Nanobeam X-Ray Scattering: Probing Matter at the Nanoscale*. Singapore: Wiley-VCH; 2013. 284 p
- [7] Monteiro WA, editor. *Neutron Scattering*. Croatia: InTech; 2016. 151 p. DOI: 10.5772/60694
- [8] McStas—a Neutron Ray-Trace Simulation Package [Internet]. Available from: <http://www.mcstas.org> [Accessed: Thu Oct 05 15:03:20 2017]
- [9] FullProf Suite [Internet]. Available from: <https://www.ill.eu/sites/fullprof/index.html> [Accessed: Thu Oct 05 15:03:20 2017]

- [10] Ariga K. *Manipulation of Nanoscale Materials: An Introduction to Nanoarhitectonics*. Great Britain: RSC Publishing; 2012. 473 p. DOI: 10.1039/9781849735124
- [11] Alguero M, Gregg JM, Mitoseriu L, editors. *Nanoscale Ferroelectrics and Multiferroics*. India: Wiley; 2016. 984 p
- [12] Bica I, Anitas EM, Chirigiu L, Bunoiu M, Juganaru I, Tatu RF. Magnetodielectric effects in hybrid magnetorheological suspensions. *Journal of Industrial and Engineering Chemistry*. 2015;**22**:53-62. DOI: 10.1016/j.jiec.2014.06.024
- [13] Bica I, Anitas EM, Averis LME. Influence of magnetic field on dispersion and dissipation of electric field of low and medium frequencies in hybrid magnetorheological suspensions. *Journal of Industrial and Engineering Chemistry*. 2015;**27**:334-340. DOI: 10.1016/j.jiec.2014.09.047
- [14] Bica I, Anitas EM, Averis LME. Tensions and deformations in composites based on polyurethane elastomer and magnetorheological suspension: Effects of the magnetic field. *Journal of Industrial and Engineering Chemistry*. 2015;**28**:86-90. DOI: 10.1016/j.jiec.2015.02.003
- [15] Newkome GR, Wang P, Moorefield CN, Cho TJ, Mohapatra PP, Li S, Hwang SH, Lukoyanova O, Echegoyen L, Palagallo JA, Iancu V, Hla SW. Nanoassembly of a fractal polymer: A molecular "Sierpinski hexagonal Gasket". *Science*. 2006;**312**:1782-1785. DOI: 10.1126/science.1125894
- [16] Cerofolini GF, Narducci D, Amato P, Romano E. Fractal nanotechnology. *Nanoscale Research Letters*. 2008;**3**:381-385. DOI: 10.1007/s11671-008-9170-0
- [17] Mayama H, Tsuji K. Menger sponge-like fractal body created by a novel template method. *The Journal of Chemical Physics*. 2006;**125**:124706. DOI: 10.1063/1.2336200
- [18] Berenschot EJW, Jansen HV, Tas NR. Fabrication of 3D fractal structures using nanoscale anisotropic etching of single crystalline silicon. *Journal of Micromechanics and Microengineering*. 2013;**23**:055024. DOI: 10.1088/0960-1317/23/5/055024
- [19] Guinier A, Fournet G. *Small-Angle Scattering of X-Rays*. New York: John Wiley & Sons; 1955. 263 p
- [20] Brumberger H, editor. *Modern Aspects of Small-Angle Scattering*. New York: NATO ASI Series; 1995. 463 p
- [21] Feigin LA, Svergun DI. *Structure Analysis by Small-Angle X-Ray and Neutron Scattering*. New York and London: Plenum Press; 1987. 335 p
- [22] Franke D, Petoukhov MV, Konarev PV, Panjkovich A, Tuukkanen A, Mertens HDT, Kikhney AG, Hajizadeh NR, Franklin JM, Jeffries CM, Svergun DI. ATSAS 2.8: A comprehensive data analysis suite for small-angle scattering from macromolecular solutions. *Journal of Applied Crystallography*. 2017;**50**:1-14. DOI: 10.1107/S1600576717007786
- [23] Craus ML, Islamov AK, Anitas EM, Cornei N, Luca D. Microstructural, magnetic and transport properties of La_{0.5}Pr_{0.2}Pb_{0.3}-xSr_xMnO₃ manganites. *Journal of Alloys and Compounds*. 2014;**592**:121-126. DOI: 10.1016/j.jallcom.2014.01.002

- [24] Heller WT. Small-angle neutron scattering and contrast variation: A powerful combination for studying biological structures. *Journal of Applied Crystallography*. 2010;**D66**:1213-1217. DOI: 10.1107/S0907444910017658
- [25] Gabel F, Lensink MF, Clantin B, Jacob-Dubuisson F, Villeret V, Ebel C. Probing the conformation of FhaC with small-angle neutron scattering and molecular Modeling. *Biophysical Journal*. 2014;**107**:185-196. DOI: 10.1016/j.bpj.2014.05.025
- [26] Zemb T, Lindner P. *Neutron, X-Rays and Light. Scattering Methods Applied to Soft Condensed Matter*. The Netherlands: North Holland; 2002. 552 p
- [27] Martin JE, Hurd AJ. Scattering from fractals. *Journal of Applied Crystallography*. 1987;**20**:61-78. DOI: 10.1107/S0021889887087107
- [28] Schmidt PW. Small-angle scattering studies of disordered, porous and fractal systems. *Journal of Applied Crystallography*. 1991;**24**:414-435. DOI: 10.1107/S0021889891003400
- [29] Cherny AY, Anitas EM, Osipov VA, Kuklin AI. Deterministic fractals: Extracting additional information from small-angle scattering data. *Physical Review E*. 2011;**83**:036203. DOI: 10.1103/PhysRevE.84.036203
- [30] Anitas EM. Small-angle scattering from fat fractals. *European Physical Journal B*. 2014;**87**:139. DOI: 10.1140/epjb/e2014-41066-9
- [31] Cherny AY, Anitas EM, Osipov VA, Kuklin AI. Small-angle scattering from multiphase fractals. *Journal of Applied Crystallography*. 2014;**47**:198-206. DOI: 10.1107/S1600576713029956
- [32] Anitas EM. Microscale fragmentation and small-angle scattering from mass fractals. *Advances in Condensed Matter Physics*. 2015;**2015**:5. ID 501281. DOI: 10.1155/2015/501281
- [33] Anitas EM. A structural model for scattering intensities with multiple fractal regions of variable length. *Journal of Optoelectronics and Advanced Materials*. 2015;**17**:1122-1127
- [34] Anitas EM. Scattering structure factor from fat fractals. *Romanian Journal of Physiology*. 2015;**60**:647-652
- [35] Cherny AY, Anitas EM, Osipov VA, Kuklin AI. The structure of deterministic mass, surface and multi-phase fractals from small-angle scattering data. *Romanian Journal of Physiology*. 2015;**60**:658-663
- [36] Anitas EM, Osipov VA, Kuklin AI, Cherny AY. Influence of randomness on small-angle scattering from deterministic mass fractals. *Romanian Journal of Physiology*. 2015;**61**:457-463
- [37] Cherny AY, Anitas EM, Osipov VA, Kuklin AI. Scattering from surface fractals in terms of composing mass fractals. *Journal of Applied Crystallography*. 2017;**50**:919-931. DOI: 10.1107/S1600576717005696
- [38] Cherny AY, Anitas EM, Osipov VA, Kuklin AI. Small-angle scattering from the cantor surface fractal on the plane and the Koch snowflake. *Physical Chemistry Chemical Physics*. 2017;**19**:2261-2268. DOI: 10.1039/C6CP07496K

- [39] Anitas EM, Slyamov A, Todoran R, Szakacs Z. Small-angle scattering from Nanoscale fat fractals. *Nanoscale Research Letters*. 2017;**12**:389. DOI: 10.1186/s11671-017-2147-0
- [40] Anitas EM, Slyamov A. Structural characterization of chaos game fractals using small-angle scattering analysis. *PLoS One*. DOI: 10.1371/journal.pone.0181385
- [41] Sandru A. Fractal structures for optical applications feasible with 2D nanotechnology. *Journal of Modern Optics*. 2012;**59**:199-204. DOI: 10.1080/09500340.2011.624646
- [42] Shang J, Wang Y, Chen M, Dai J, Zhou X, Kuttner J, Hilt G, Shao X, Wu K. Assembling molecular Sierpinski triangle fractals. *Nature Chemistry*. 2015;**7**:389-393. DOI: 10.1038/nchem.2211
- [43] Loh ND, Hampton CY, Martin AV, Starodub D, Sierra RG, Barty A, Aquila A, Schulz J, Lomb L, Steinbrener J, et al. Fractal morphology, imaging and mass spectrometry of single aerosol particles in flight. *Nature*. 2012;**486**:513-517. DOI: 10.1038/nature11222
- [44] Debye P. Zerstreung von Röntgenstrahlen. *Annalen der Physik*. 1915;**46**:809-823. DOI: 10.1002/andp.19153510606
- [45] Pantos E, van Garderen HF, Hilbers PAJ, Beelen TPM, van Santen RA. Simulation of small-angle scattering from large assemblies of multi-type scatterer particles. *Journal of Molecular Structure*. 1996;**383**:303-306. DOI: 10.1016/S0022-2860(96)09302-7
- [46] Barnsley M. *Fractals Everywhere*. USA: Dover Publications; 2012. 560 p
- [47] Wolfram S. Statistical mechanics of cellular automata. *Reviews of Modern Physics*. 1983;**55**:601-644. DOI: 10.1103/RevModPhys.55.601
- [48] Wolfram S. Universality and complexity in cellular automata. *Physica D: Nonlinear Phenomena*. 1984;**10**:1-35. DOI: 10.1016/0167-2789(84)90245-8
- [49] Wolfram S. *A New Kind of Science*. USA: Wolfram Media; 2002. 1192 p

IntechOpen

